

Low-loss on-chip superconducting microwave circulator assisted by shunting capacitors

N. Pradeep Kumar,^{*} Dat Thanh Le,^{*} Prasanna Pakkiam, Thomas M. Stace[✉], and Arkady Fedorov
Analog Quantum Circuits Pty. Ltd., Brisbane, QLD 4066, Australia
and School of Mathematics and Physics, University of Queensland, Brisbane, QLD 4072, Australia

 (Received 28 May 2024; accepted 9 December 2024; published 21 January 2025)

Ferrite-free circulators that are passive and readily integratable on a chip are highly sought-after in quantum technologies based on superconducting circuits. In our previous work, we implemented such a circulator using a three-Josephson-junction loop that exhibited unambiguous nonreciprocity and signal circulation, but required junction energies to be within 1% of design values. This tolerance is tighter than standard junction fabrication methods provide, so we propose and demonstrate a design improvement that relaxes the required junction fabrication precision, allowing for higher device performance and fabrication yield. Specifically, we introduce large direct capacitive couplings between the waveguides, which based on the modeling we describe here, requires less stringent junction fabrication tolerance. We implement the design, and measure enhanced “circulation fidelity” above 97%, with optimized on-resonance insertion loss of 0.2 dB, isolation of 18 dB, and power reflectance of -15 dB, in good agreement with model calculations.

DOI: [10.1103/PhysRevResearch.7.013075](https://doi.org/10.1103/PhysRevResearch.7.013075)

I. INTRODUCTION

Circulators are a paradigmatic example of nonreciprocal devices with a wide use in telecommunication and microwave electronics [1–3]. They are also indispensable for cryogenic microwave measurements where they are used to route weak microwave signals while protecting the system of interest from thermal noise caused by higher temperature stages [4,5]. However, conventional ferrite circulators are bulky and not compatible with microfabrication nor with superconducting circuits, and thus unsuitable for very-large-scale superconducting microwave networks. Given the drive to scale up superconducting quantum computers, designs for integrated microwave circulators on a chip are becoming critical [6,7].

Many approaches to integrating circulators with other solid-state quantum circuits involve the application of strong magnetic fields, either real or synthesized with time-dependent control fields [4,8–25]. However, these approaches may also be incompatible with microfabricated superconducting systems, or add AC-control complexity.

In contrast, our recent results demonstrated the realization of an on-chip superconducting circulator with only passive (i.e., DC) control [26,27], based on a three-Josephson-junction loop [28,29]. While nonreciprocity and microwave circulation were evident [27], the device performance was limited by asymmetry in Josephson junction energies. In particular, the device exhibited a ‘circulation fidelity’ of $\sim 80\%$ (i.e., the fidelity of the measured device scattering matrix relative to that of an ideal circulator) corresponding to an insertion

loss of 2 dB, when post-selected on a specific quasiparticle configuration sector.

In this paper, we report the implementation of an improved design for a three-junction circulator device, which has been analysed in Refs. [26–30]. As in earlier work, the core of the device comprises three superconducting islands, indicated by different colors in Fig. 1(a) that are connected to each other via Josephson junctions, and are capacitively coupled to external waveguides. The key advance reported here is the inclusion of shunt capacitors that directly couple the waveguides [23,24,31], indicated as C_X in Fig. 1(a). This introduces an additional microwave scattering pathway, giving rise to multipath interference, analogous to Fano scattering [32,33].

Our theoretical simulations of the proposed design predict that high circulation fidelity, above 97% (corresponding to an insertion loss of 0.2 dB), can be reached even when the spread in the Josephson energies is $\sim 3\%$, which is achievable with standard electron beam lithography [34,35]. We confirm our theoretical predictions with experimental measurements, demonstrating significantly enhanced circulation performance.

As with previously reported devices, our experimental system still suffers from significant quasiparticle hopping, so we use postselection to characterize and optimize the device performance within a single quasiparticle sector. Relative to Fedorov *et al.* [27], in Sec. IV D, we report a tenfold improvement in device performance, with measured insertion loss of $IL = 0.2$ dB, isolation of $IS = 18$ dB, and power reflectance of $R = -15$ dB at resonance. Section IV C provides a rough upper bound on internal device losses of < 0.4 dB.

II. BACKGROUND

The electronic design of the capacitively shunted circulator is shown in Fig. 1(a). Figure 1(b) implements this device, with the capacitive shunts included in the hexagonal structure

^{*}These authors contributed equally to this work.

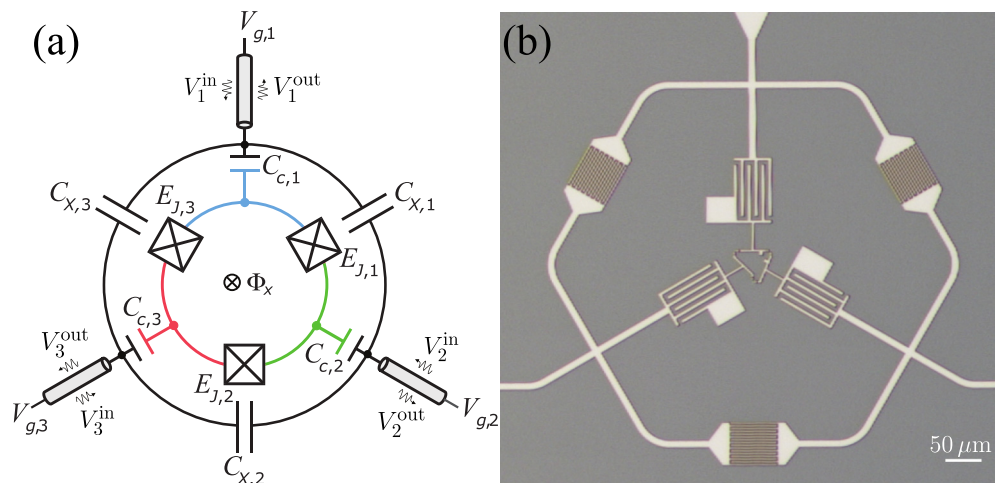


FIG. 1. (a) Lumped-element circuit model of the capacitively shunted circulator. The device consists of three Josephson junctions arranged in a loop that creates three superconducting islands (indicated by blue, green, and red colors). The islands are capacitively coupled to external waveguides via C_c , and the waveguides are also directly coupled to one-another by capacitive shunts C_x . (b) Optical microscope image of a fabricated device, where the centered triangle represents the loop formed by three Josephson junctions and the outer ring represents the inter-waveguide capacitances.

linking the waveguides, which couple to off-chip signal sources and analysers. The experimental setup is described in detail in Sec. IV.

To measure the scattering response of the system, we drive it with input voltage signals V_j^{in} and measure the output voltage signals V_j^{out} scattered by the device to determine the scattering matrix amplitudes $S_{ji} = V_j^{\text{out}}/V_i^{\text{in}}$ with $i, j \in \{1, 2, 3\}$. We use an external DC flux bias threaded through the junction loop and DC charge biases applied to the superconducting islands [Φ_x and $V_{g,(1,2,3)}$ in Fig. 1(a)] to control the operation of the device.

Given the device's scattering matrix S , we quantify its circulation performance by defining the average clockwise and anticlockwise circulation fidelities, and the average reflection respectively as

$$\mathcal{F}_\circlearrowright = (|S_{13}| + |S_{32}| + |S_{21}|)/3, \quad (1a)$$

$$\mathcal{F}_\circlearrowleft = (|S_{12}| + |S_{23}| + |S_{31}|)/3, \quad (1b)$$

$$\mathcal{R} = (|S_{11}| + |S_{22}| + |S_{33}|)/3. \quad (1c)$$

An ideal clockwise circulator will have $\mathcal{F}_\circlearrowright = 1$ and $\mathcal{F}_\circlearrowleft = \mathcal{R} = 0$ [27].

Our earliest experimental implementation of the three-junction-loop circulator (without shunt capacitors) was reported in Navarathna *et al.* [26], where we observed qualitative nonreciprocal behavior, i.e., $S_{ij} \neq S_{ji}$ for $i \neq j$, albeit with a low circulation fidelity $\sim 50\%$. Based on detailed modeling, we attributed this low circulation performance to electrical asymmetry in the Josephson junctions, which had a large relative spread in Josephson energies $\delta E_J \sim 8.5\%$, where $\delta E_J \equiv (\max_j[E_{J,j}] - \min_j[E_{J,j}])/\bar{E}_{J,j}$.

This stems from the fact that a large value of δE_J determines the frequency splitting between the nearly degenerate first and second excited states of the loop. The interference of scattering pathways mediated by these states is responsible for signal circulation in the device [30], so that when this splitting is much larger than the waveguide coupling strength, an

external drive cannot simultaneously couple strongly to both of the excited states, thus limiting the nonreciprocal interference.

Furthermore, the device reported in Ref. [26] was sensitive to charge fluctuations. In particular, quasiparticle tunneling between the superconducting islands created four quasiparticle sectors, each with a distinct scattering response [30]. The average quasiparticle lifetime of the device in Ref. [26] was found to be $\tau^{(\text{qp})} \sim 200 \mu\text{s}$.

The second iteration of the three-junction-loop circulator reported in Fedorov *et al.* [27] (also without shunt capacitors) featured a more geometrically symmetric design with a smaller spread in Josephson energies $\delta E_J \sim 2.2\%$. Additional design optimization ensured that the capacitance matrix of the system was electrically symmetric. With these improvements, the device showed significant nonreciprocity and reached circulation fidelity $\sim 80\%$ (postselected over quasiparticle sectors), for both clockwise and counterclockwise circulation. The average quasiparticle lifetime was also improved to $\tau^{(\text{qp})} \sim 4 \text{ ms}$, due to enhanced infrared shielding and a change in electronic parameters to reduce the charge-parity-switching rates.

To attain higher circulation performance in the three-junction system investigated in Ref. [27], modeling predicted that we need $\delta E_J \lesssim 1\%$ [30], which is more constrained than standard junction fabrication precision allows for. Instead, this level of precision can only be reliably assured with post-fabrication treatments such as laser annealing [36].

In the following sections, we demonstrate an alternative approach to improving the circulation performance, based on Fano-like interference arising from the inclusion of shunt capacitors. The inspiration for this approach follows earlier work which considered shunt capacitances (either stray or engineered) as important elements of circulators [23,24,31]. We first develop a detailed theoretical model of the system, and use this to show that including relatively large waveguide shunt capacitors in the circulator design relaxes the required

junction fabrication precision, so that circulation becomes more robust against variations in Josephson junction energies. We then implement the device design, shown in Fig. 1(b), to demonstrate the experimental performance of the system, confirming good agreement between theory and experiment, as well as high quality circulation, after accounting for quasiparticle noise.

III. MODELING AND ANALYSIS

In this section, we develop a theoretical input-output model, which we use to show that introducing direct capacitive couplings between the waveguides, as shown in Fig. 1(a), enhances the circulation fidelity close to the ideal, even when asymmetry in Josephson energies is relatively large.

A. SLH master equation

We derive a master equation for a three-junction loop capacitively coupled to input-output waveguides, including direct waveguide shunt capacitors mutually coupling the waveguides. We begin by first describing the bare Hamiltonian of the junction loop [28–30]

$$\begin{aligned} \hat{H}_{\text{loop}} = & E_{C_\Sigma} \left((\hat{n}'_1 - \frac{1}{2}(n_0 + n_{g,1} - n_{g,3}))^2 \right. \\ & + (\hat{n}'_2 + \frac{1}{2}(n_0 + n_{g,2} - n_{g,3}))^2 - \hat{n}'_1 \hat{n}'_2 \\ & - E_{J,1} \cos(\hat{\phi}'_1 - \frac{1}{3}\phi_x) - E_{J,2} \cos(\hat{\phi}'_2 - \frac{1}{3}\phi_x) \\ & \left. - E_{J,3} \cos(\hat{\phi}'_1 + \hat{\phi}'_2 + \frac{1}{3}\phi_x), \right) \end{aligned} \quad (2)$$

which depends on a single charging energy E_{C_Σ} (under the assumption that the system capacitances are symmetric), three Josephson energies $E_{J,j}$, three charge biases $n_{g,j}$, and a flux bias ϕ_x . In Eq. (2), the charge operators \hat{n}'_1 and \hat{n}'_2 , the conserved total charge n_0 , and the phase (difference) operators $\hat{\phi}'_1$ and $\hat{\phi}'_2$ are related to the original charge and phase operators of the superconducting islands as follows, $\hat{n}'_1 = \hat{n}_1$, $\hat{n}'_2 = -\hat{n}_2$, $n_0 = \hat{n}_1 + \hat{n}_2 + \hat{n}_3$, $\hat{\phi}'_1 = \hat{\phi}_1 - \hat{\phi}_3$, and $\hat{\phi}'_2 = \hat{\phi}_3 - \hat{\phi}_2$. The form of the kinetic (charging) energy in Eq. (2) implies that the loop Hamiltonian \hat{H}_{loop} actually depends on the relative bias charges between the islands, $n_{g,1} - n_{g,3}$ and $n_{g,2} - n_{g,3}$. Therefore, tuning two charge biases only, e.g., $n_{g,1}$ and $n_{g,2}$, as well as the flux bias ϕ_x suffices to control the total operation of the circulator device. In terms of its eigenbasis $\{|k\rangle; k = 0, 1, 2, \dots\}$, \hat{H}_{loop} is expressed as $\hat{H}_{\text{loop}} = \sum_{k \geq 1} \hbar \omega_k |k\rangle \langle k|$, where ω_k is the loop transition frequency from the ground state $|0\rangle$ to the excited state $|k\rangle$ ($k \geq 1$).

We consider injecting single-mode weak coherent fields with coherent amplitudes $\langle \hat{\mathbf{a}}^{\text{in}} \rangle = (\alpha_1, \alpha_2, \alpha_3)^\top$ at a drive frequency ω_d to the three waveguide ports. Following the ‘‘Scattering-Lindblad-Hamiltonian’’ (SLH) formalism [37], we model the coherent input fields, the coupled waveguides, and the junction loop as three cascaded systems with their SLH triples respectively given by

$$G_d = (\mathbb{1}_{3 \times 3}, \hat{\mathbf{L}}_d, 0), \quad (3)$$

$$G_{\text{wg}} = (\mathbf{A}, 0, 0), \quad (4)$$

$$G_{\text{loop}} = (\mathbb{1}_{3 \times 3}, \hat{\mathbf{L}}_{\text{loop}}, \hat{H}_{\text{loop}}), \quad (5)$$

where $\hat{\mathbf{L}}_d = (\alpha_1 \hat{\mathbf{L}}, \alpha_2 \hat{\mathbf{L}}, \alpha_3 \hat{\mathbf{L}})^\top$ denotes the coupling operators associated with the input drive fields and $\hat{\mathbf{L}}_{\text{loop}} = (\sqrt{\Gamma} \hat{q}_{1,-}, \sqrt{\Gamma} \hat{q}_{2,-}, \sqrt{\Gamma} \hat{q}_{3,-})^\top$ denotes the coupling operators associated with the junction loop. Here Γ is the coupling strength between the junction loop and the waveguides and $\hat{q}_{j,-} = \sum_{k < \ell} \langle k | \hat{q}_j | \ell \rangle |k\rangle \langle \ell|$ are the upper triangularized parts (in the junction loop eigenbasis) of the operators \hat{q}_j , where $\hat{q}_1 = \hat{n}'_1$, $\hat{q}_2 = -\hat{n}'_2$, and $\hat{q}_3 = -\hat{n}'_1 + \hat{n}'_2$.

G_d and G_{loop} represent three-port systems, while G_{wg} represents a six-port scattering system, with three ‘‘exterior’’ and three ‘‘interior’’ ports; its 6×6 scattering matrix \mathbf{A} is derived in Appendix A. As analysed in Appendix B, the ‘‘interior’’ ports of G_{wg} are connected to the ports of G_{loop} in a feedback configuration. We therefore apply both the SLH series and feedback rules [37] to cascade the total drive-waveguide-loop SLH triple

$$G_{\text{tot}} = G_d \triangleleft (G_{\text{wg}} \leftrightarrow G_{\text{loop}}), \quad (6)$$

which collectively describes a three-port device. Here we have introduced a new SLH composition notation, $A \leftrightarrow B$ to indicate that systems A (outer) and B (inner) are coupled in a feedback loop. Equation (6) is the basis for the SLH modeling, and further details are provided in Appendix B, and illustrated in Fig. 7(c).

Given G_{tot} , the Lindblad master equation for the density operator ρ of the loop system in a frame rotating at the drive frequency ω_d is given by

$$\dot{\rho} = -i[\hat{H}'_{\text{tot}}, \rho] + \sum_{j=1}^3 \mathcal{D}[\hat{a}_j^{\text{out}}] \rho, \quad (7)$$

where $\mathcal{D}[\hat{\rho}] = \frac{1}{2}(2\hat{\rho}\hat{\rho}^\dagger - \hat{\rho}\hat{\rho}^\dagger - \hat{\rho}^\dagger\hat{\rho})$ and

$$\hat{H}'_{\text{tot}} = \hat{H}'_{\text{loop}} + \hat{H}_s + \hat{H}_d, \quad (8)$$

$$\hat{\mathbf{a}}^{\text{out}} = \hat{\mathbf{L}}_{w \leftarrow 1} + S_{w \leftarrow 1} \hat{\mathbf{L}}_d. \quad (9)$$

Here $\hat{H}'_{\text{loop}} = \sum_{k \geq 1} (\omega_k - \omega_d) |k\rangle \langle k|$, \hat{H}_s and \hat{H}_d represent the frequency shifts and the driving fields to the junction loop system, $\hat{\mathbf{a}}^{\text{out}} = (\hat{a}_1^{\text{out}}, \hat{a}_2^{\text{out}}, \hat{a}_3^{\text{out}})^\top$ denotes the output fields, and $\hat{\mathbf{L}}_{w \leftarrow 1}$ and $S_{w \leftarrow 1}$ are the coupling operators and the scattering matrix of the feedback-reduced cascaded system $G_{\text{wg}} \leftrightarrow G_{\text{loop}}$. Explicit expressions of the operators in Eqs. (8) and (9) are given in Appendix B. Since $V_j^{\text{in}} = K \alpha_j$ and $V_j^{\text{out}} = K(\hat{a}_j^{\text{out}})$, where K is a conversion factor and $\langle \hat{O} \rangle = \text{Tr}(\hat{O} \rho)$, the scattering matrix S with its elements $S_{ji} = V_j^{\text{out}} / V_i^{\text{in}} = \langle \hat{a}_j^{\text{out}} \rangle / \alpha_i$ can be computed numerically from Eqs. (7) and (9).

B. Reduced sensitivity to junction asymmetry

The inclusion of the waveguide shunt capacitors modifies the scattering mechanism in the proposed circulator. In particular, in Appendix C, we adiabatically eliminate the loop degrees of freedom to approximate the system scattering matrix, at low drive powers, as $S = (\mathbb{1} + R_{\text{loop}}) \cdot S_{w \leftarrow 1}$, where R_{loop} represents the response of the junction loop to the external drives. This shows that scattering of the whole capacitively shunted-waveguide and junction-loop system is mediated via two pathways, namely, a direct pathway represented by the

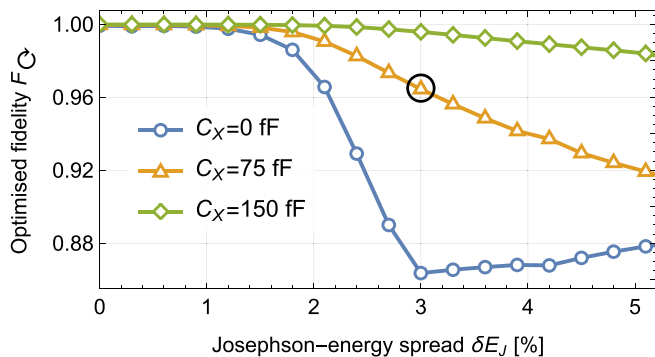


FIG. 2. Optimized circulation fidelity, \mathcal{F}_\circ , as a function of the Josephson-energy spread δE_J for increasing values of the interwaveguide capacitances, $C_X = \{0, 75, 150\}$ fF. The fidelity is computed from the scattering matrix S computed with the master equation in Eq. (7). The junction loop parameters are $E_{C_\Sigma}/h = 3.09$ GHz and $E_{J,2} = 15.03$ GHz, and we allow variations in $E_{J,1/3}$ as $E_{J,1} = E_{J,2}(1 - \delta E_J/2)$, and $E_{J,3} = E_{J,2}(1 + \delta E_J/2)$. The black circle marks the point where $\delta E_J = 3\%$, $C_X = 75$ fF, yielding an optimized fidelity $\mathcal{F}_\circ \gtrsim 97\%$, which is consistent with the measured circulation fidelity in Fig. 5.

waveguide scattering $S_{w \leftrightarrow 1}$ and the loop-mediated scattering represented by R_{loop} . This gives rise to the Fano-like multipath interference effect with asymmetric line shapes in the transmission and reflection spectra [32,33].

In what follows, we provide numerical evidence that the waveguide shunt capacitors reduce the sensitivity of the circulation fidelity to variations in the Josephson junctions fabricated in the loop. To this end, we numerically solve the master equation in Eq. (7), compute the output fields, and determine the scattering matrix S .

For simulation purposes, we take $E_{C_\Sigma}/h = 3.09$ GHz, $E_{J,2}/h \equiv E_J/h = 15.03$ GHz to match experimental parameters discussed in Sec. IV, following, and we allow $E_{J,1/3}$ to vary as $E_{J,1} = E_J(1 - \delta E_J/2)$, and $E_{J,3} = E_J(1 + \delta E_J/2)$, where δE_J is the fractional spread in junction energies. For $0 \leq \delta E_J \leq 5\%$, we numerically optimize the flux and charge biases, and the drive frequency to find the optimal clockwise circulation fidelity at each δE_J . This “maximally asymmetric” choice of junction energies for $E_{J,1/3}$ relative to the mean value E_J represents the worst-case-scenario circulation fidelity [30], so provides an estimate of the worst-case effect of asymmetry on the circulation performance.

The simulation results are shown in Fig. 2, where we plot the optimized circulation fidelity, \mathcal{F}_\circ , as a function of the Josephson-energy spread δE_J for three values of the inter-waveguide capacitances $C_X \in \{0, 75, 150\}$ fF. We observe that for small junction spread, the fidelity is high, i.e., $\mathcal{F}_\circ \approx 1$ for $\delta E_J \lesssim 1\%$, regardless of the value of C_X . For larger asymmetry, the fidelity improves with increasing C_X . In particular, the curve for $C_X = 75$ fF, which corresponds to our experimental value, shows high circulation performance up to $\delta E_J \sim 3\%$. These simulations indicate that large interwaveguide capacitances substantially enhance the robustness of the circulation fidelity against Josephson-junction asymmetry.

IV. EXPERIMENTAL RESULTS

A. Device fabrication and measurement

The device shown in Fig. 1(b) was composed of four layers of aluminium deposited on a high resistivity silicon wafer with different thicknesses to reduce quasiparticle tunneling by gap engineering [38]. The first layer of 100 nm formed the capacitors and the basic structure of the junction loop. Standard double-angle evaporation was then used to deposit two layers of aluminium, of 20 nm and 60 nm respectively, with a single oxidation step between the two aluminium deposition stages to form three Josephson junctions. A final “patch” layer was deposited to ensure electrical continuity within each island. After evaporation, the chip was diced and bonded on a holder suitable for cryogenic measurements in a dilution refrigerator operating at a base temperature of 10 mK.

The device was characterized using a fast, room-temperature microwave switch to sequentially direct the external drive to each of the three input ports for 100 μs , and measuring the response at the three output ports with a vector network analyser (VNA), as shown in Fig. 3, which yields a column of the scattering matrix. To extract the full 3×3 scattering matrix, we switch between the inputs, for a total cycle time of $\tau_s = 300 \mu\text{s}$.

B. Spectral response

We first measured the spectral response of the system as a function of the magnetic flux in the junction loop provided by a small external coil mounted on the bottom of the sample holder. In Fig. 4, the measured spectrum, which features a characteristic Y-shape [26,27,29,30], shows good agreement with the theoretical model, and the fitting provides an estimate for the electronic parameters of the device.

Specifically, the model fitting returns an on-site charging energy $E_{C_\Sigma}/h = (2e)^2/(hC_\Sigma) = 3.09$ GHz, which corresponds to a total island capacitance of $C_\Sigma = C_g + C_C + 3C_J = 37.5$ fF, where C_g , C_C , and C_J are the ground, waveguide-loop coupling, and junction capacitances respectively. This is close to the design value of $C_\Sigma = 40$ fF, from designed capacitance values $C_g = 2.3$ fF, $C_C = 27.5$ fF, and $C_J = 3.5$ fF. The fitted values for the Josephson energies are $E_{J,(1,2,3)}/h = \{14.73, 15.15, 15.22\}$ GHz with a spread $\delta E_J = 3.2\%$. These values are reasonably consistent with the measured room-temperature junction resistances $R_{J,(1,2,3)} = \{6.86, 7, 7.02\}$ k Ω [39], noting that junction resistances may drift slightly, relative to one-another, over several days.

C. Scattering analysis

We next measured the full 3×3 complex-valued scattering matrix S .

The raw data obtained at the VNA include the response of the scattering matrix S of the capacitively shunted on-chip circulator, along with the attenuation, amplification, and loss inside the cabling in the dilution refrigerator. To isolate the device scattering matrix, S , we use a two-step calibration procedure, which we describe briefly here. A more detailed description is provided in Appendix E.

In the first, coarse calibration step, we use three radial microwave switches at the mixing chamber stage inside the

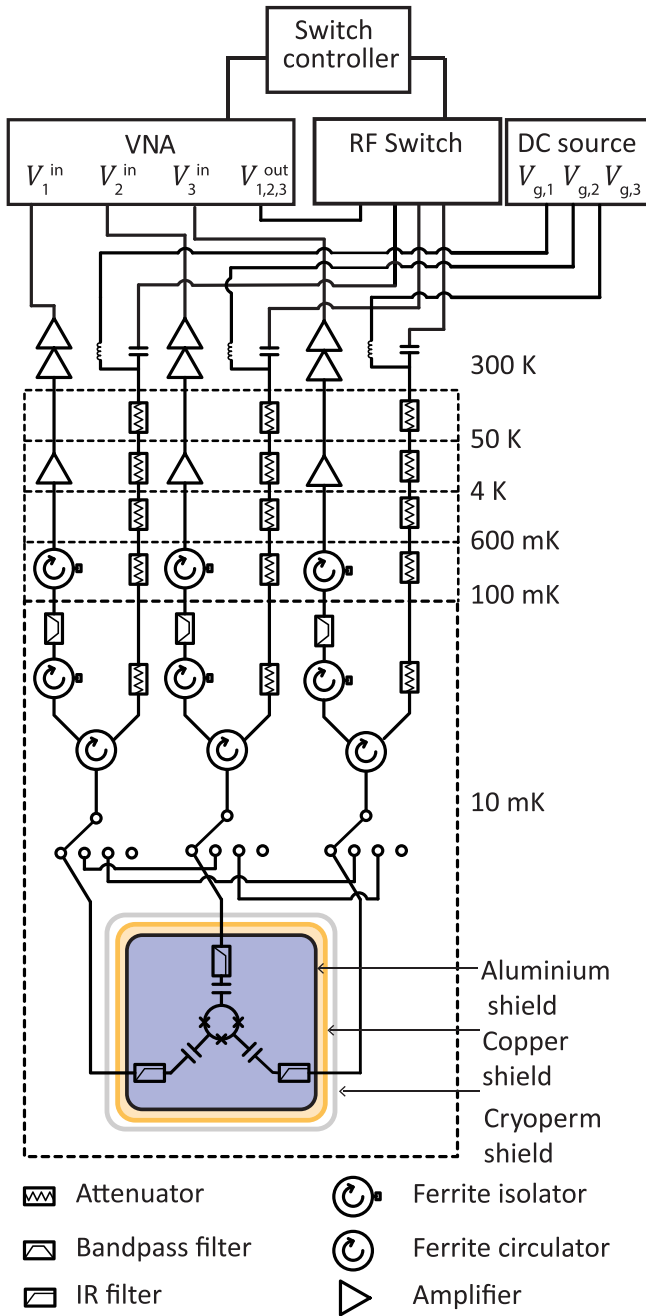


FIG. 3. Circuit diagram of the experimental setup inside the dilution refrigerator. The ports of the device are connected to radial microwave switches to allow for bypassing the device and calibrating the input and output lines. The inputs V_j^{in} are sent through attenuators to the device. DC voltages $V_{g,j}$ are added to the RF input lines via bias tees at room temperature. Each of the outputs V_j^{out} from the device goes through an IR-filter, a circulator, two isolators, a band pass filter, a HEMT amplifier, and room temperature amplifiers.

dilution refrigerator (see Fig. 3), which allow us to bypass the device and measure direct transmission through all the possible combinations of the input and output lines. Assuming that the lines were matched to 50Ω and there were no reflections at the switches, we calibrated the transfer functions of the cables and amplifiers up to the magnetic shield of

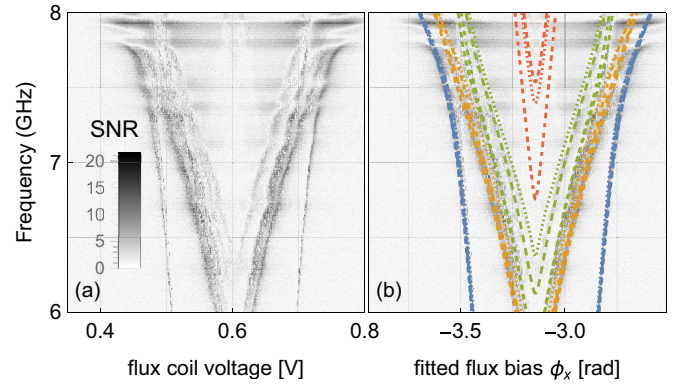


FIG. 4. (a) Spectral response for voltage scattering from port 1 to port 2 while sweeping over the flux coil voltage. The raw voltage output at each frequency is scaled so that the far-off-resonant background data (i.e., where the flux coil voltage is < 0.4 V) has zero mean and unit variance; the gray-scale thus represents the output signal-to-noise ratio of $|S_{21}|$. (b) Fitted model spectral lines superimposed on the measured spectrum, including four distinct quasiparticle sectors; the model spectrum obscures the experimental features across the flux and frequency scan, indicating high quality agreement between theory and experiment. The horizontal features in the data are attributed to weak resonances from reflections in the cabling. The fitting process also converts the dimensional flux coil voltage into a dimensionless flux bias $\phi_x = 2\pi\Phi_x/\Phi_0$. Different colors correspond to transition frequencies from the ground state to the first excited state (blue), second (orange), third (green), and fourth (red). The fourfold multiplet within the fitted spectrum is due to four quasiparticle sectors.

the device [27], yielding an input attenuation matrix \mathcal{A} and output amplification matrix \mathcal{B} , which are described in detail in Appendix E.

In the second, fine calibration step, we fitted the coarsely calibrated data to a model which accounts for additional losses within the magnetic shield induced predominantly by inline infra-red (IR) filters shown in Fig. 3. These filters are inherently outside of the coarse calibration step. This process yielded both the device scattering matrix, S , that represents the device response, as well as an additional attenuation matrix, \mathcal{C} , quantifying the IR-filter absorption (see Appendix E for details). As an independent validation of this fine calibration, the fitted IR filter attenuation matrix \mathcal{C} corresponds to a single-pass attenuation of 1.4 dB, which is close to the expected value of 1 dB at 7 GHz, inferred from the manufacturer’s data sheet. The difference of 0.4 dB between these figures is a rough upper bound for the internal device losses.

The sampling time for each scattering matrix measurement was $\tau_s = 300 \mu s$. As in our previous work [26,27], we observed the characteristic jumps between discrete output voltage states which are classified and attributed to four different quasiparticle sectors with a K -means classifier. The results of the quasiparticle analysis and classification reported here exactly replicate the process we developed and described in Ref. [27]. The typical characteristic dwell times for the four quasiparticle sectors were measured as $\tau_{1,2,3,4}^{(qp)} = \{3.48, 3.61, 4.23, 3.14\}$ ms, which is comparable to those in our previous device [27]. This classification then allowed us

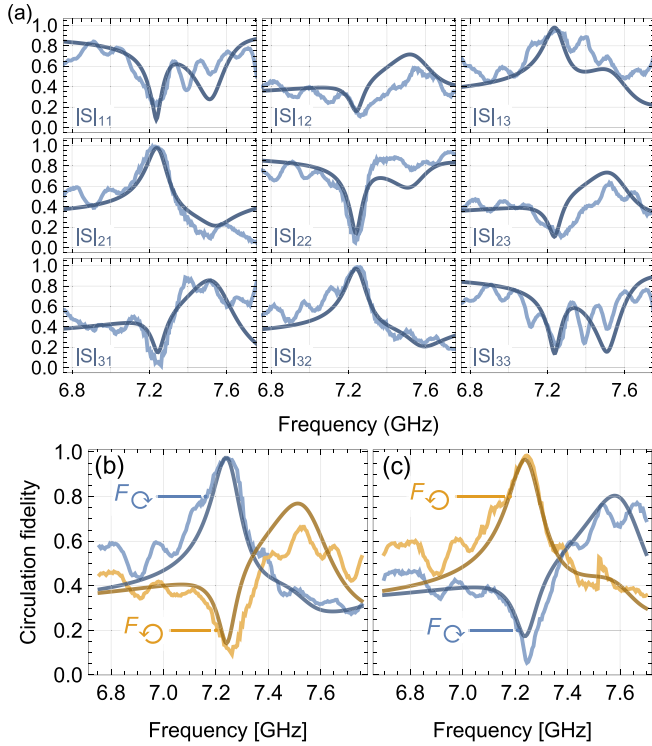


FIG. 5. (a) Spectra of optimized clockwise-circulating S -matrix elements. We note the small oscillations with period ~ 200 MHz are likely due to weak reflections in the cabling, described in Appendix F. (b) Clockwise and counterclockwise fidelities for this set of S -matrix data. (c) Clockwise and counterclockwise fidelities of the S -matrix data optimally biased for counterclockwise circulation, showing that circulation direction in the device can be changed electronically.

to compute the circulation fidelity in each of the four quasiparticle sectors. We then tuned the charge and flux biases to maximize the measured fidelity for one of the quasiparticle sectors. Fixing these biases at a working point with a high circulation fidelity, we measured the scattering matrix S while scanning over the drive frequency.

The extracted scattering matrix S of the device in the optimized sector is shown in Fig. 5(a) (lighter-colored), where we see strong nonreciprocity with $|S_{12}| \ll |S_{21}|$, $|S_{23}| \ll |S_{32}|$, and $|S_{31}| \ll |S_{13}|$ around 7.25 GHz. In addition, we observe asymmetric line shapes, which are indicative of multipath Fano-like interference, as well as noticeable background oscillations in some of the scattering matrix elements, which we attribute to weak etalon resonances arising from back-reflection in the cabling (see Appendix F for more details).

We also show in Fig. 5(a) the results of model simulations (darker-colored), where we used the same device parameters obtained from the spectral fit in Fig. 4 to compute the theoretical scattering matrix. The scattering matrix fit yields a value of the inter-waveguide capacitance $C_X = 76$ fF, which is reasonably close to the design value from finite-element electrostatic simulations (84 fF). The fit also returns the waveguide-loop coupling strength of 270 MHz, which is roughly double the value in Fedorov *et al.* [27] due to a larger design ratio C_C/C_Σ [30].

In Fig. 5(b), we show the clockwise and counterclockwise circulation fidelities, \mathcal{F}_\circ and \mathcal{F}_\ominus defined in Sec. 1, of the measured scattering spectrum in Fig. 5(a) (lighter-colored), along with the theoretical fidelities (darker-colored). The peak clockwise circulation fidelity measured in Fig. 5(b) is $\mathcal{F}_\circ = 0.97$ with a correspondingly small counterclockwise circulation fidelity of $\mathcal{F}_\ominus = 0.12$, showing significant clockwise signal circulation. This is consistent with the theoretical simulations in Fig. 2, where we predict that at a Josephson-energy spread $\delta E_J = 3.2\%$ circulation fidelity $\mathcal{F} > 0.96$ is achievable for a waveguide shunt capacitance of $C_X \sim 75$ fF.

The direction of signal circulation in our device can be dynamically switched with the external voltage control biases. Figure 5(c) shows the fidelities \mathcal{F}_\circ and \mathcal{F}_\ominus versus the drive frequency at a voltage-bias tuned for counterclockwise circulation; the results look very similar to those in Fig. 5(b), except their roles are exchanged. The peak counterclockwise circulation fidelity measured in Fig. 5(c) is $\mathcal{F}_\ominus = 0.98$, and $\mathcal{F}_\circ = 0.05$ is correspondingly small.

For completeness, we present the scattering matrices for the other quasiparticle sectors in Appendix D. As in Ref. [27], the clockwise circulation performance in the other, unoptimized quasiparticle sectors is significantly worse than the sector reported in Fig. 5(a).

D. Circulation performance and power dependence

We analyze the device performance as a clockwise circulator by defining the average insertion loss IL, the average isolation IS, and the average power reflectance R respectively as

$$\text{IL} = \mathcal{F}_\circ^2, \quad \text{IS} = \mathcal{F}_\ominus^2, \quad \text{R} = \mathcal{R}^2. \quad (10)$$

These quantities are computed from the scattering data in Fig. 5(a) and are shown in Fig. 6(a), where we find that at the resonance frequency 7.25 GHz, $\text{IL} = 0.2$ dB, $\text{IS} = 18$ dB, and $\text{R} = -15$ dB. In addition, Fig. 6(a) shows $\text{IL} < 1$ dB over a bandwidth of 90 MHz, while $\text{IS} > 14$ dB over a bandwidth of 85 MHz. The circulator device studied here thus exhibits a tenfold improvement in the insertion loss relative to the earlier device reported in [27] (for which $\text{IL} = 2$ dB, $\text{IS} = 14$ dB, and $\text{R} = -11$ dB at resonance). Based on the model predictions shown in Fig. 2, we attribute this to the inclusion of the shunt capacitors, which reduces the required junction fabrication precision.

Finally, to complete the characterization of the device performance we measured the saturation power. In Fig. 6(b), we show the dependence of the measured counterclockwise fidelity on the input signal power (at an off-resonance drive frequency 7.46 GHz), as well as including numerical simulations. The 3 dB compression point is $P_{3\text{dB}} \approx -126$ dBm, which is the same as in our previous circulator device [27].

Microwave circulation in the device arises from quantum interference between the ground and excited states of the junction loop. The junction-loop energy spectrum is strongly anharmonic, and so we expect the device saturation power to correspond to the arrival of one drive photon per excited-state lifetime, $\tau_e = (\Gamma \|\langle e | \hat{n}_a | g \rangle\|^2)^{-1}$. Using our fitted device parameters, we find $\Gamma \approx 270$ MHz and $\|\langle e | \hat{n}_a | g \rangle\|^2 \approx 0.3$, which

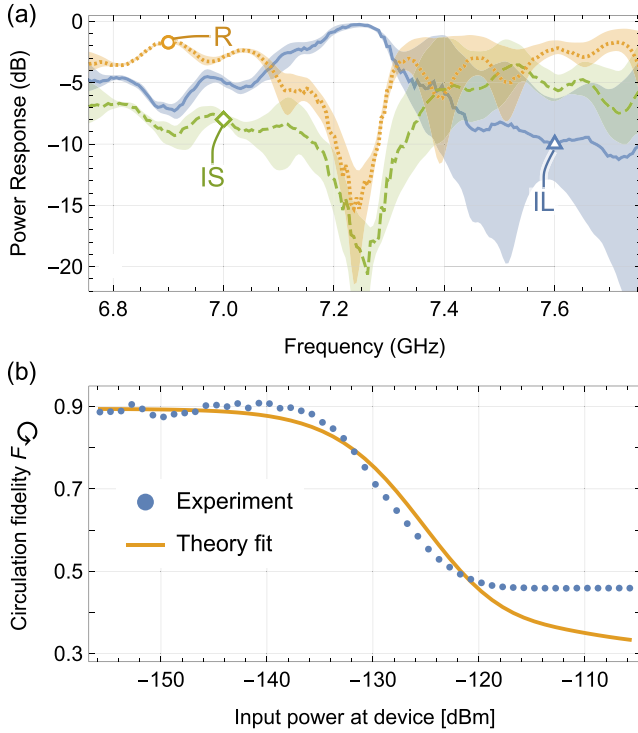


FIG. 6. (a) Clockwise circulation performance for the scattering data in Fig. 5(a), including the average insertion loss $IL = \mathcal{F}_{\odot}^2$, the average isolation $IS = \mathcal{F}_{\ominus}^2$, and the average power reflectance $R = \mathcal{R}^2$. The range of each curve indicated by a shaded region is computed from the smoothed maxima and minima over the terms in the corresponding definition in Sec. 1. (b) Counterclockwise fidelity \mathcal{F}_{\ominus} at an off-resonant drive frequency 7.46 GHz as a function of the input power obtained from both theory and experiment, showing the saturation power of about $P_{3dB} \approx -126$ dBm.

implies a saturation power $P_{\text{sat}} \approx hf/\tau_e = -124$ dBm, consistent with the experimentally measured value for P_{3dB} above.

V. DISCUSSION AND CONCLUSIONS

In this work, we analysed an improved design for an on-chip superconducting circulator based on a three-Josephson-junction loop. The key advance over our earlier results [26–29] was the addition of shunt capacitors between the input-output waveguides to induce Fano-like interference between the scattering pathways. We showed theoretically and experimentally that circulation in the capacitively shunted, three-junction loop is substantially less sensitive to Josephson junction asymmetry and exhibits notable improvement in the circulation performance.

This simple design modification increased the tolerable junction asymmetry to $\delta E_J \lesssim 3\%$, removing the need for additional fabrication post-processing to fine-tune the Josephson junctions towards higher symmetry. The approach may also be applicable to other multicomponent interference devices in reducing the sensitivity to typical imprecision in component fabrication.

The device insertion loss, isolation, and return loss, which are postselected on the optimized quasiparticle sector, are

comparable to the performance of commercial ferrite circulators. The measured bandwidth, though not as large as in commercial devices, is already sufficient for some practical applications, for example, single qubit readout [40]. However, the saturation power and the nonequilibrium quasiparticles, which cause random switching into and out of the high-performance sector, remain barriers to making the device practically useful.

ACKNOWLEDGMENTS

This work was funded through a commercial research contract with Analog Quantum Circuits (AQC) Pty. Ltd. T.M.S. and A.K. each declare a financial interest in AQC. The authors acknowledge assistance from the Centre for Microscopy and Microanalysis at the University of Queensland, and the Australian National Fabrication Facility, ANFF-Q.

APPENDIX A: SCATTERING BETWEEN CAPACITIVELY COUPLED WAVEGUIDES

We decompose the circuit model in Fig. 1(a) into a system of capacitively coupled waveguides and the three-junction loop. The waveguide system shown Fig. 7(a) has three “exterior” input/output ports denoted by $\mathbf{a}^{\text{in/out}} = (a_1^{\text{in/out}}, a_2^{\text{in/out}}, a_2^{\text{in/out}})^T$ that couple to external fields, and three “interior” input/output ports denoted by $\mathbf{b}^{\text{in/out}} = (b_1^{\text{in/out}}, b_2^{\text{in/out}}, b_2^{\text{in/out}})^T$ that couple to the junction loop. The exterior ports couple to each other via the shunt waveguide capacitors $C_{X,j} \equiv C_X$ and couple to the interior ports via coupling capacitors $\tilde{C}_{C,j} \equiv \tilde{C}_C$. Later calculations will take the limit $\tilde{C}_C \rightarrow \infty$ to account for the actually galvanic connection between the exterior and interior ports.

In the following, we derive the 6×6 scattering matrix \mathbf{A} for the system of waveguides in Fig. 7(a). We assume that they are capacitively connected to each other at the end points $x = 0$. Following the theory of lossless semi-infinite waveguides in Ref. [41], the voltage and current at the end point $x = 0$ of the waveguide a_j (or b_j), denoted respectively as V_{a_j/b_j} and I_{a_j/b_j} , are given by

$$V_{a_j/b_j} = V_{a_j/b_j}^{\text{out}} + V_{a_j/b_j}^{\text{in}}, \quad (\text{A1})$$

$$I_{a_j/b_j} = \frac{V_{a_j/b_j}^{\text{out}} - V_{a_j/b_j}^{\text{in}}}{Z_{\text{wg}}}, \quad (\text{A2})$$

where V_{a_j/b_j}^{out} and V_{a_j/b_j}^{in} are the output and input voltages, and Z_{wg} is the waveguide impedance.

We apply Kirchoff’s current law at the coupling points $x = 0$ of the waveguides a_j and b_j and find that

$$I_{a_j} + \frac{V_{b_j} - V_{a_j}}{Z_{\tilde{C}_j}} + \sum_{j' \neq j} \frac{V_{a_{j'}} - V_{a_j}}{Z_{C_{j,j'}}} = 0, \quad (\text{A3})$$

$$I_{b_j} + \frac{V_{a_j} - V_{b_j}}{Z_{\tilde{C}_j}} = 0, \quad (\text{A4})$$

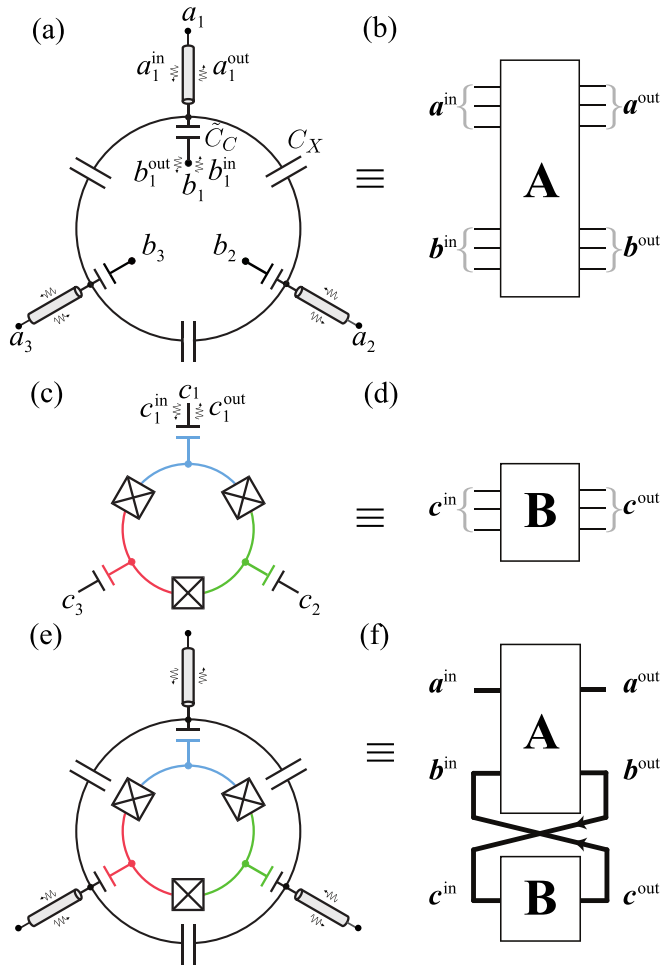


FIG. 7. We describe the (a) capacitively coupled waveguides. Formally, we take $\tilde{C}_C \rightarrow \infty$, to compute the transfer matrix for $a^{\text{in}} \rightarrow b^{\text{out}}$. (b) The 6×6 scattering matrix \mathbf{A} from Eq. (A9), relating the triplets of input and output modes of the capacitive shunts, where $a^{\text{in/out}} = (a_1^{\text{in/out}}, a_2^{\text{in/out}}, a_3^{\text{in/out}})$ are the ‘‘exterior’’ inputs and outputs to/from the waveguides, and $b^{\text{in/out}}$ are the ‘interior’ input and output modes to/from the junction loop. The junction loop (c) is described by (d) a 3×3 junction loop scattering matrix \mathbf{B} relating the loop input modes, c^{in} , to the loop output modes, c^{out} , as well as the internal Hamiltonian evolution of the loop degrees of freedom. The scattering matrix for the (e) waveguide-loop system from Fig. 1 is described by the SLH formalism in which \mathbf{A} and \mathbf{B} are coupled in a feedback loop, shown in (f), with the internal modes constrained so that $b^{\text{out}} = c^{\text{in}}$ and $b^{\text{in}} = c^{\text{out}}$ [37]. The heavier lines indicate triplets of modes. Not shown here is the scattering system of the external coherent drives that couple to the exterior ports of the waveguides.

where $Z_{C_{j,j'}} = 1/i\omega_d C_X$ and $Z_{\tilde{C}_j} = 1/i\omega_d \tilde{C}_C$. Using Eqs. (A1) and (A2), we rewrite Eqs. (A3) and (A4) in terms of V_{a_j/b_j}^{out} and V_{a_j/b_j}^{in}

$$\frac{V_{a_j}^{\text{out}} - V_{a_j}^{\text{in}}}{Z_{\text{wg}}} + \frac{V_{b_j}^{\text{out}} + V_{b_j}^{\text{in}} - V_{a_j}^{\text{out}} - V_{a_j}^{\text{in}}}{Z_{\tilde{C}_j}} + \sum_{j' \neq j} \frac{V_{a_{j'}}^{\text{out}} + V_{a_{j'}}^{\text{in}} - V_{a_j}^{\text{out}} - V_{a_j}^{\text{in}}}{Z_{C_{j,j'}}} = 0, \quad (\text{A5})$$

$$\frac{V_{b_j}^{\text{out}} - V_{b_j}^{\text{in}}}{Z_{\text{wg}}} + \frac{V_{a_j}^{\text{out}} + V_{a_j}^{\text{in}} - V_{b_j}^{\text{out}} - V_{b_j}^{\text{in}}}{Z_{\tilde{C}_j}} = 0. \quad (\text{A6})$$

These equations can be concisely represented in matrix form

$$[\mathbb{1} + i\omega_d Z_{\text{wg}} \mathbf{C}] \begin{bmatrix} V_a^{\text{out}} \\ V_b^{\text{out}} \end{bmatrix} = [\mathbb{1} - i\omega_d Z_{\text{wg}} \mathbf{C}] \begin{bmatrix} V_a^{\text{in}} \\ V_b^{\text{in}} \end{bmatrix}, \quad (\text{A7})$$

where $V_{a/b}^{\text{in/out}} = (V_{a_1/b_1}^{\text{in/out}}, V_{a_2/b_2}^{\text{in/out}}, V_{a_3/b_3}^{\text{in/out}})$, and the full 6×6 capacitance matrix,

$$\mathbf{C} = \begin{bmatrix} C_X - C_\Sigma & C_C \\ C_C & -C_C \end{bmatrix}, \quad (\text{A8})$$

is defined in terms of the 3×3 partial capacitance matrices $C_\Sigma = (\tilde{C}_C + 2C_X)\mathbb{1}$, $C_C = \tilde{C}_C\mathbb{1}$, and

$$C_X = \begin{bmatrix} 0 & C_X & C_X \\ C_X & 0 & C_X \\ C_X & C_X & 0 \end{bmatrix}.$$

We solve Eq. (A7) to obtain the shunt capacitor scattering matrix,

$$\mathbf{A} = [\mathbb{1} + i\omega_d Z_{\text{wg}} \mathbf{C}]^{-1} \cdot [\mathbb{1} - i\omega_d Z_{\text{wg}} \mathbf{C}], \quad (\text{A9})$$

$$\equiv \begin{bmatrix} A_{11} & A_{12} \\ A_{21} & A_{22} \end{bmatrix},$$

which implicitly defines the 3×3 submatrices A_{ij} . This scattering matrix is represented graphically in Fig. 7(b). We take the limit $\tilde{C}_C \rightarrow \infty$ and define $z = \omega_d Z_{\text{wg}} C_X$, so that

$$A_{11} = A_{22} = \frac{z}{2i + 3z} \begin{bmatrix} -2 & 1 & 1 \\ 1 & -2 & 1 \\ 1 & 1 & -2 \end{bmatrix},$$

$$A_{12} = A_{21} = \frac{z}{2i + 3z} \begin{bmatrix} 1 + \frac{2i}{z} & 1 & 1 \\ 1 & 1 + \frac{2i}{z} & 1 \\ 1 & 1 & 1 + \frac{2i}{z} \end{bmatrix}.$$

APPENDIX B: SLH MASTER EQUATION

We use the SLH formalism [37] to model the input-output network in our device. It consists of the external coherent drives, the coupled waveguides, and the junction loop. The drives are modeled as a three-port component following the source model; its SLH triple is given by

$$G_d = (\mathbb{1}_{3 \times 3}, \hat{\mathbf{L}}_d, 0), \quad (\text{B1})$$

where $\hat{\mathbf{L}}_d = (\alpha_1 \hat{\mathbb{1}}, \alpha_2 \hat{\mathbb{1}}, \alpha_3 \hat{\mathbb{1}})^\top$ with α_j the drive amplitudes. The coupled waveguides are a six-port component without any coupling operators nor system Hamiltonian with its SLH triple of the form

$$G_{\text{wg}} = (\mathbf{A}, 0, 0), \quad (\text{B2})$$

where \mathbf{A} is given in Eq. (A9). The junction loop depicted in Figs. 7(c) and 7(d) is a three-port component represented by an SLH triple

$$G_{\text{loop}} = (\mathbb{1}_{3 \times 3}, \hat{\mathbf{L}}_{\text{loop}}, \hat{\mathbf{H}}_{\text{loop}}), \quad (\text{B3})$$

where $\hat{\mathbf{L}}_{\text{loop}} = (\sqrt{\Gamma}\hat{q}_{1,-}, \sqrt{\Gamma}\hat{q}_{2,-}, \sqrt{\Gamma}\hat{q}_{3,-})^\top$ and \hat{H}_{loop} is given in the main text.

The total network is cascaded as

$$G_{\text{tot}} = G_{\text{d}} \triangleleft G_{\text{w} \leftarrow 1}, \quad (\text{B4})$$

where $G_{\text{w} \leftarrow 1} = G_{\text{wg}} \leftrightarrow G_{\text{loop}}$ describes the feedback loop concatenation between the interior ports of G_{wg} and the ports of G_{loop} , as described in Figs. 7(e) and 7(f). We compute $G_{\text{w} \leftarrow 1}$ by first cascading $G_{\text{w} \leftarrow 1} = G_{\text{wg}} \triangleleft (G_3 \boxplus G_{\text{loop}})$, where $G_3 = (\mathbf{1}, 0, 0)$ and find that

$$G_{\text{w} \leftarrow 1} = \left(\mathbf{A}, \begin{bmatrix} 0 \\ \hat{\mathbf{L}}_{\text{loop}} \end{bmatrix}, \hat{H}_{\text{loop}} \right). \quad (\text{B5})$$

$G_{\text{w} \leftarrow 1}$ has six ports: its ‘‘upper’’ ports denoted as 1 do not involve any coupling operators and its ‘‘lower’’ ports denoted as 2 correspond to $\hat{\mathbf{L}}_{\text{loop}}$ and are looped back to themselves. We then use the feedback rule to eliminate these internal degrees of freedom. The reduced three-port waveguide-loop SLH triple $G_{\text{w} \leftarrow 1} = [G_{\text{w} \leftarrow 1}]_{2 \leftrightarrow 2}$ is given by

$$S_{\text{w} \leftarrow 1} = \mathbf{A}_{11} + \mathbf{A}_{12}(\mathbf{1} - \mathbf{A}_{22})^{-1}\mathbf{A}_{21}, \quad (\text{B6a})$$

$$\hat{\mathbf{L}}_{\text{w} \leftarrow 1} = \mathbf{A}_{12}(\mathbf{1} - \mathbf{A}_{22})^{-1}\hat{\mathbf{L}}_{\text{loop}}, \quad (\text{B6b})$$

$$\hat{H}_{\text{w} \leftarrow 1} = \hat{H}_{\text{loop}} - \frac{i}{2}(\hat{\mathbf{L}}_{\text{loop}}^\dagger \mathbf{A}_{22}(\mathbf{1} - \mathbf{A}_{22})^{-1}\hat{\mathbf{L}}_{\text{loop}} - \text{H.c.}). \quad (\text{B6c})$$

Finally, the total SLH triple G_{tot} in Eq. (B4) is

$$S_{\text{tot}} = S_{\text{w} \leftarrow 1}, \quad (\text{B7a})$$

$$\hat{\mathbf{L}}_{\text{tot}} = \hat{\mathbf{L}}_{\text{w} \leftarrow 1} + S_{\text{w} \leftarrow 1}\hat{\mathbf{L}}_{\text{d}}, \quad (\text{B7b})$$

$$\hat{H}_{\text{tot}} = \hat{H}_{\text{w} \leftarrow 1} - \frac{i}{2}(\hat{\mathbf{L}}_{\text{w} \leftarrow 1}^\dagger S_{\text{w} \leftarrow 1}\hat{\mathbf{L}}_{\text{d}} - \text{H.c.}). \quad (\text{B7c})$$

We decompose \hat{H}_{tot} as $\hat{H}_{\text{tot}} = \hat{H}_{\text{loop}} + \hat{H}_{\text{s}} + \hat{H}_{\text{d}}$, where

$$\hat{H}_{\text{s}} = -\frac{i}{2}(\hat{\mathbf{L}}_{\text{loop}}^\dagger \mathbf{A}_{22}(\mathbf{1} - \mathbf{A}_{22})^{-1}\hat{\mathbf{L}}_{\text{loop}} - \text{H.c.}), \quad (\text{B8a})$$

$$\hat{H}_{\text{d}} = -\frac{i}{2}(\hat{\mathbf{L}}_{\text{w} \leftarrow 1}^\dagger S_{\text{w} \leftarrow 1}\hat{\mathbf{L}}_{\text{d}} - \text{H.c.}), \quad (\text{B8b})$$

which respectively describe the frequency shifts and the driving to \hat{H}_{loop} . Given these, we obtain the master equation for the junction loop’s density operator (in a rotating frame at the

drive frequency ω_{d})

$$\dot{\rho} = -i[\hat{H}'_{\text{tot}}, \rho] + \sum_{j=1}^3 \mathcal{D}[\hat{\mathbf{L}}_{\text{tot},j}]\rho. \quad (\text{B9})$$

Equation (B7b) in fact is nothing but the input-output relation, where $\hat{\mathbf{L}}_{\text{tot}} \equiv \hat{\mathbf{a}}^{\text{out}}$, $\hat{\mathbf{L}}_{\text{w} \leftarrow 1}$, and $S_{\text{w} \leftarrow 1}\hat{\mathbf{L}}_{\text{d}}$ represent the output fields, the system’s response, and the input fields, respectively. This reproduces the master equation Eq. (7) in the main text. We note that when $C_X = 0$, one finds $\hat{H}_{\text{s}} = 0$ and $S_{\text{w} \leftarrow 1} = \mathbf{1}$, which reduces Eq. (B9) or (7) to the SLH master equation used in Refs. [26,27,29,30].

APPENDIX C: ADIABATIC ELIMINATION

We consider a semianalytical derivation for the scattering matrix S via adiabatic elimination of the SLH triple [37], which provides us useful insights into the operation of the proposed circulator. In particular, we assume that the drive fields are weak so that the junction-loop system is mostly populated in its ground state [29]. This allows us to separate the Hilbert space of the loop into a fast subspace $\mathcal{F} = \{|k\rangle, k \geq 1\}$ that contains its excited states and a slow subspace $\mathcal{S} = \{|0\rangle\}$ that contains only its ground state. We then eliminate the dynamics of the fast subspace while considering only that of the slow subspace (for more details, see Appendix B in Ref. [30]). By doing so, we find that the scattering matrix S within the slow subspace is given by

$$S = (\mathbf{1} + R_{\text{loop}}).S_{\text{w} \leftarrow 1}, \quad (\text{C1})$$

where R_{loop} represents the response of the junction loop to the external coherent drives. We note that a similar expression to Eq. (C1) was derived in Ref. [42] for a resonator coupled to multiple ports in the presence of a direct scattering channel between the ports. The matrix elements of R_{loop} are [30]

$$(R_{\text{loop}})_{ij} = -\sum_{k>0} \frac{\langle 0|\hat{\mathbf{L}}_{\text{w} \leftarrow 1,i}|k\rangle \langle k|\hat{\mathbf{L}}_{\text{w} \leftarrow 1,j}|0\rangle}{i\Delta\omega_k + \Gamma_k/2}, \quad (\text{C2})$$

where $\Delta\omega_k = \omega_k - \omega_{\text{d}}$ and $\Gamma_k = \langle k|\hat{\mathbf{L}}_{\text{loop}}^\dagger \mathbf{A}_{\text{s}}\hat{\mathbf{L}}_{\text{loop}}|k\rangle$, with $\mathbf{A}_{\text{s}} = \mathbf{A}_{22}(\mathbf{1} - \mathbf{A}_{22})^{-1}$. Here Γ_k represents the waveguide-induced decay rate as well as the frequency shift of the excited state $|k\rangle$. We numerically confirm that the S-matrices computed via the full SLH master equation (7) and via adiabatic elimination Eq. (C1) agree very well with each other.

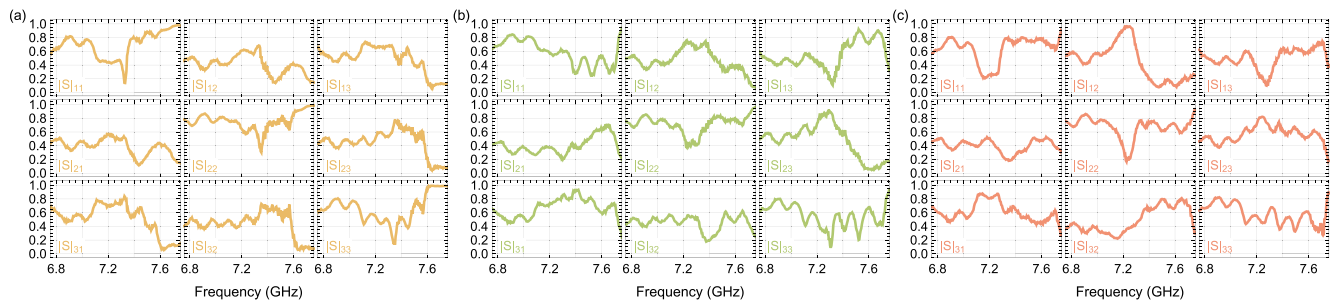


FIG. 8. Scattering matrices of the other three quasiparticle sectors, obtained from the same data analysis that produced the scattering matrix in Fig. 5(a) with high clockwise circulation. The (clockwise) circulation performance in each of these sectors is substantially worse than in the optimized sector.

APPENDIX D: SCATTERING MATRICES OF OTHER QUASIPARTICLE SECTORS

In Fig. 8, we show the measured scattering matrices for the other quasiparticle sectors obtained from the same data analysis that yielded the scattering matrix reported in Fig. 5(a). The clockwise circulation performance is evidently poor for these, compared with the best sector in Fig. 5(a).

APPENDIX E: CALIBRATION OF THE SCATTERING MATRIX

Here we provide more detail on the two-step calibration process we used to measure the device scattering matrix S from the raw scattering matrix data, M . The calibration assumes that M is determined by attenuation on the three input lines, \mathcal{A} , amplification on the three output lines, \mathcal{B} , the “bare” device scattering matrix S and high-pass IR-filters on each port of the device \mathcal{C} , which contribute about 1 dB of attenuation per pass. The attenuation and amplification matrices \mathcal{A} , \mathcal{B} , and \mathcal{C} are assumed to be diagonal in the port labels (i.e., no cable cross-talk). Formally, we assume that the measured scattering matrix is given by

$$M = \mathcal{B} \cdot \mathcal{C} \cdot S \cdot \mathcal{C} \cdot \mathcal{A}. \tag{E1}$$

The cabling layout is shown schematically in Fig. 9. Using a bypass switch installed inside the fridge, we are able to directly calibrate \mathcal{A} and \mathcal{B} , to provide a “coarse” calibration. The high-pass IR filter is necessarily installed after the bypass switch, and so it cannot be directly calibrated. Instead, we use fitting to provide a “fine” calibration to simultaneously determine \mathcal{C} and S .

In the first, coarse calibration step, the bypass switches are used to directly connect the input and output lines, with which we extract the input and output attenuation matrices $\mathcal{A} = \text{diag}(a_1, a_2, a_3)$ and $\mathcal{B} = \text{diag}(b_1, b_2, b_3)$ of the cables and the amplifiers between the fridge exterior and the magnetic shielding inside the fridge. This requires nine different switch settings to access the different combinations of $a_i b_j$. One example of the bypass switch setting is shown in Fig. 9, where we measure input line $i = 1$ (red), and output line $j = 3$ (blue), giving us $a_1 b_3$. Typically there is about 135 dB of attenuation in the input lines, and 87 dB of amplification in the output lines.

Given raw 3×3 device scattering matrix data, M , at some frequency, and a complete set of the bypass switch measurement, we compute the coarsely calibrated scattering matrix $\tilde{S} = \mathcal{B}^{-1} \cdot M \cdot \mathcal{A}^{-1}$. Example data for \tilde{S} are shown in Fig. 10(a). The coarse calibration assumes only that \mathcal{A} and \mathcal{B} are diagonal. We find that \tilde{S} is not unitary, since it still includes residual attenuation from the in-line IR filters and cabling inside the shields.

To account for the IR-filter attenuation, we perform a second, fine calibration, where we assume that S is very close to being a 3×3 unitary matrix, parameterized as U_3 . This assumption reflects our belief, based on our modeling, that the superconducting device has very low internal losses; we check this assumption against the expected IR-filter attenuation, described below. We perform least-squares fitting over

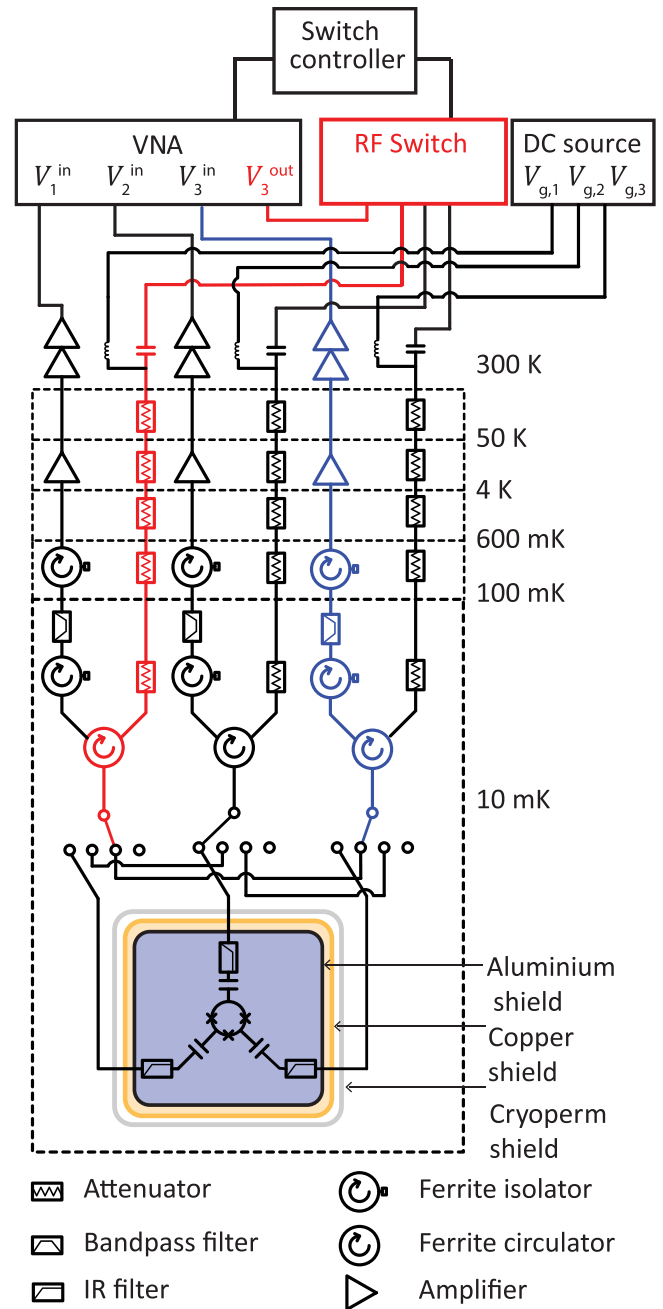


FIG. 9. The schematic wiring diagram of the input and output lines to the device, shown in a bypass configuration. Bypass switches are used to directly connect the input and output lines, in different combinations, bypassing the device. Shown here, input line $i = 1$ (red) is connected to output line $j = 3$ (blue). The various switch configurations yield the transfer product $a_i b_j$ for the input and output lines, which can be measured as a function of frequency. This provides the coarse in-situ calibration described in Appendix E.

the parameterized U_3 and $\mathcal{C} = \text{diag}(c_1, c_2, c_3)$ to minimize the residuals of $|U_3 - \mathcal{C}^{-1} \cdot \tilde{S} \cdot \mathcal{C}^{-1}|$. The fitting process simultaneously yields in-situ IR-filter attenuation parameters c_j and a “pure” unitary device scattering matrix U_3 . Finally, we use \mathcal{C} as the fine calibration factor required to compute the “bare” scattering matrix of the device, $S = \mathcal{C}^{-1} \cdot \tilde{S} \cdot \mathcal{C}^{-1}$.

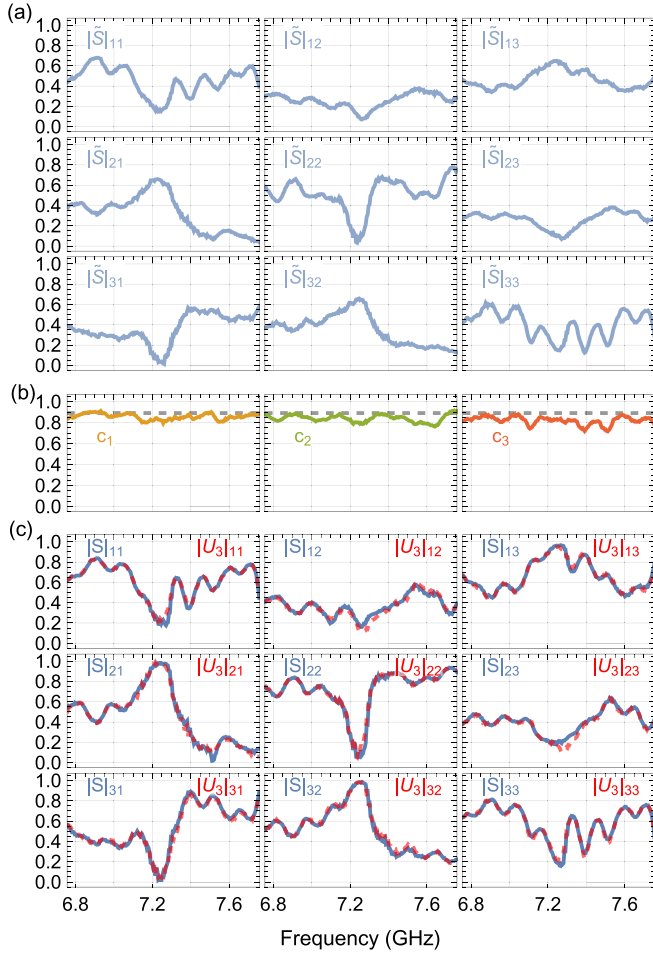


FIG. 10. (a) Coarsely calibrated scattering matrix $\tilde{S} = B^{-1} \cdot M \cdot A^{-1}$ that corrects the raw scattering matrix M with the calibrated transfer functions A (attenuation) and B (amplification) of the cables and amplifiers outside of the magnetic shield. A and B are determined using bypass switches. (b) The fitted loss matrix $C = \text{diag}(c_1, c_2, c_3)$ that represents the additional line losses within the magnetic shield, caused mainly by the in-line IR filters. The fitted values are not strongly dependent on the frequency. The extracted IR-filter attenuation of approximately 0.85 (1.4 dB) is consistent with the estimated value 1 dB ($c_j \approx 10^{-(1 \text{ dB})/20} \approx 0.89$) from the manufacturer's specification sheet, shown by the dashed line. (c) The finely calibrated scattering matrix $S = C^{-1} \cdot \tilde{S} \cdot C^{-1}$ (solid blue) obtained by correcting the coarsely calibrated data with the fitted IR-filter attenuation. We see that S is very close to the nearest 3×3 unitary approximation U_3 for the device scattering matrix (dashed red). The blue curves showing S in this panel are the same as in Fig. 5(a).

Figure 10(b) shows the values of c_j extracted from \tilde{S} . We see that the $c_j \approx 0.85$ (i.e., attenuation of 1.4 dB) do not depend strongly on the drive frequency over the band shown. This corresponds closely to the expected ~ 1 dB attenuation (i.e., $10^{-1/20} = 0.89$ in amplitude) shown as dashed lines in Fig. 10(b), inferred from the IR-filter manufacturer's data sheet [43]. The 0.4 dB difference between the fitted absorption and the IR-filter specification provides a rough upper bound on the internal losses in the device. Given variations in each IR-filter, the true internal losses of the circulator may be substantially smaller than 0.4 dB.

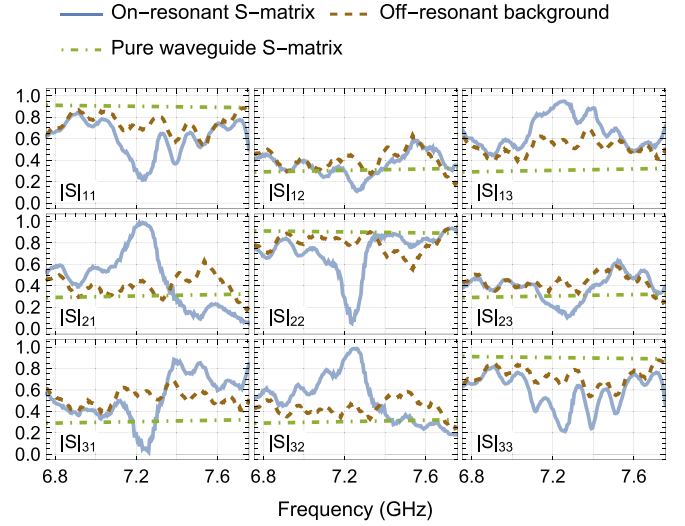


FIG. 11. Comparison of the on-resonant scattering matrix data (solid blue) in Fig. 5(a) with the off-resonant background response (dashed brown), showing very similar oscillations away from the resonant frequency 7.25 GHz. Also shown is the computed shunt-capacitor scattering amplitudes (dot-dashed green) from Eq. (B7a), assuming $C_X = 75.7$ fF. We attribute the period ~ 200 MHz to weak reflections in cabling, over a length of about 0.5 m.

The bare device scattering matrix, $S = C^{-1} \cdot \tilde{S} \cdot C^{-1}$, is shown in Fig. 10(c) (blue), compared with the pure unitary matrix U_3 extracted from fitting (dashed red). We see that S and U_3 are in close agreement, indicating that the coarsely calibrated data are consistent with the assumption that it is generated by a unitary scattering device with IR-filter contributing attenuation of $c_j \approx 1$ dB per pass. That is, we confirm that $\tilde{S} \approx C \cdot U_3 \cdot C$ to a good approximation.

In addition to the *in situ*, model-free calibration based on the data analysis described here, the physics-based SLH modeling shown in Fig. 5(a) also agrees well with the calibrated scattering matrix S . We note that the cabling resonances that result in small oscillations in the scattering data (see Fig. 11) are reciprocal and so cannot affect the nonreciprocal scattering of the device, including the measure of circulation fidelity.

APPENDIX F: BACKGROUND OSCILLATIONS

The S -matrix elements shown in Figs. 5(a) and 8 have noticeable oscillatory responses with peak-to-trough amplitude of about 0.2, and a characteristic period of about 200 MHz. We attribute these to weak, resonant reflections in the cabling, over a length of around $L \sim 0.5$ m, which could arise from weak reflections (with reflectivities at the level of a few percent) at co-axial connectors or other weak scattering sites. These form low- Q etalons with a free spectral range $\text{FSR} = c/(2L) \sim 200$ to 300 MHz, as seen in Fig. 11. Given the small reflectivities of a few percent involved in producing these etalons, they will be dominated by formed between pairs of scatterers (rather than multiple scattering processes). When the 3-junction device is circulating on resonance, additional multireflection interference processes could open up. However given the hypothesized few-percent reflectivities of

the weak scattering points, any additional circulator-induced etalons will be higher order, and therefore of lower amplitude.

Figure 11 reproduces the resonant circulation data (solid blue) in Fig. 5(a), as well as similar scattering data (dashed brown) taken with the flux-bias selected to fully detune the device from the frequency band shown. The on-resonance and detuned data sets were taken approximately 10 days apart, and have clear qualitative correlations in their FSRs away from resonance, but with quantitative differences which may arise from slow drifts in, e.g., the weak-reflection strength over the time between the measurements. In addition, the pure theoretical scattering matrix amplitudes for a shunt capacitor array, computed with Eq. (B7a), are shown (dot-dashed green), which broadly match the off-resonance scattering am-

plitudes, apart from the small oscillations attributed to the cable back-reflections.

We note two additional observations that suggest the etalons are partially associated to scattering from the shunt capacitors. Firstly, the background oscillations are not strongly evident in the independent calibration of the \mathcal{A} and \mathcal{B} matrices, which are measured by bypassing the device, including the shunt capacitors. A consequence of this is that the coarse calibration step described in Appendix E does not remove the background oscillations. Secondly, our earlier work [27] based on an unshunted device had much less pronounced background oscillations from etalons. Together, these observations suggest that the etalons are related to the shunt capacitors.

-
- [1] D. Pozar, *Microwave Engineering* (Wiley, New York, 2011).
- [2] X. Gu, A. F. Kockum, A. Miranowicz, Y. xi Liu, and F. Nori, Microwave photonics with superconducting quantum circuits, *Phys. Rep.* **718-719**, 1 (2017).
- [3] Y.-Y. Wang, S. van Geldern, T. Connolly, Y.-X. Wang, A. Shilcuskys, A. McDonald, A. A. Clerk, and C. Wang, Low-loss ferrite circulator as a tunable chiral quantum system, *Phys. Rev. Appl.* **16**, 064066 (2021).
- [4] A. Metelmann and A. A. Clerk, Nonreciprocal photon transmission and amplification via reservoir engineering, *Phys. Rev. X* **5**, 021025 (2015).
- [5] F. Ruesink, M.-A. Miri, A. Alù, and E. Verhagen, Nonreciprocity and magnetic-free isolation based on optomechanical interactions, *Nat. Commun.* **7**, 13662 (2016).
- [6] D. J. Reilly, Engineering the quantum-classical interface of solid-state qubits, *npj Quantum Inf.* **1**, 15011 (2015).
- [7] S. Bravyi, O. Dial, J. M. Gambetta, D. Gil, and Z. Nazario, The future of quantum computing with superconducting qubits, *J. Appl. Phys.* **132**, 160902 (2022).
- [8] B. J. Chapman, E. I. Rosenthal, J. Kerckhoff, B. A. Moores, L. R. Vale, J. A. B. Mates, G. C. Hilton, K. Lalumière, A. Blais, and K. W. Lehnert, Widely tunable on-chip microwave circulator for superconducting quantum circuits, *Phys. Rev. X* **7**, 041043 (2017).
- [9] A. Kamal, J. Clarke, and M. H. Devoret, Noiseless nonreciprocity in a parametric active device, *Nat. Phys.* **7**, 311 (2011).
- [10] A. Kamal and A. Metelmann, Minimal models for nonreciprocal amplification using biharmonic drives, *Phys. Rev. Appl.* **7**, 034031 (2017).
- [11] N. A. Estep, D. L. Sounas, J. Soric, and A. Alù, Magnetic-free non-reciprocity and isolation based on parametrically modulated coupled-resonator loops, *Nat. Phys.* **10**, 923 (2014).
- [12] K. M. Sliwa, M. Hatridge, A. Narla, S. Shankar, L. Frunzio, R. J. Schoelkopf, and M. H. Devoret, Reconfigurable Josephson circulator/directional amplifier, *Phys. Rev. X* **5**, 041020 (2015).
- [13] F. Lecocq, L. Ranzani, G. A. Peterson, K. Cicak, R. W. Simmonds, J. D. Teufel, and J. Aumentado, Nonreciprocal microwave signal processing with a field-programmable Josephson amplifier, *Phys. Rev. Appl.* **7**, 024028 (2017).
- [14] K. Fang, J. Luo, A. Metelmann, M. H. Matheny, F. Marquardt, A. A. Clerk, and O. Painter, Generalized non-reciprocity in an optomechanical circuit via synthetic magnetism and reservoir engineering, *Nat. Phys.* **13**, 465 (2017).
- [15] C. W. Peterson, W. A. Benalcazar, M. Lin, T. L. Hughes, and G. Bahl, Strong nonreciprocity in modulated resonator chains through synthetic electric and magnetic fields, *Phys. Rev. Lett.* **123**, 063901 (2019).
- [16] J. Kerckhoff, K. Lalumière, B. J. Chapman, A. Blais, and K. W. Lehnert, On-Chip superconducting microwave circulator from synthetic rotation, *Phys. Rev. Appl.* **4**, 034002 (2015).
- [17] P. Roushan, C. Neill, A. Megrant, Y. Chen, R. Babbush, R. Barends, B. Campbell, Z. Chen, B. Chiaro, A. Dunsworth, A. Fowler, E. Jeffrey, J. Kelly, E. Lucero, J. Mutus, P. J. J. O'Malley, M. Neeley, C. Quintana, D. Sank, A. Vainsencher, et al., Chiral ground-state currents of interacting photons in a synthetic magnetic field, *Nat. Phys.* **13**, 146 (2017).
- [18] E. I. Rosenthal, B. J. Chapman, A. P. Higginbotham, J. Kerckhoff, and K. W. Lehnert, Breaking Lorentz reciprocity with frequency conversion and delay, *Phys. Rev. Lett.* **119**, 147703 (2017).
- [19] B. Abdo, N. T. Bronn, O. Jinka, S. Olivadese, A. D. Córcoles, V. P. Adiga, M. Brink, R. E. Lake, X. Wu, D. P. Pappas *et al.*, Active protection of a superconducting qubit with an interferometric Josephson isolator, *Nat. Commun.* **10**, 3154 (2019).
- [20] B. Abdo, O. Jinka, N. T. Bronn, S. Olivadese, and M. Brink, High-fidelity qubit readout using interferometric directional Josephson devices, *PRX Quantum* **2**, 040360 (2021).
- [21] A. Rosario Hamann, C. Müller, M. Jerger, M. Zanner, J. Combes, M. Pletyukhov, M. Weides, T. M. Stace, and A. Fedorov, Nonreciprocity realized with quantum nonlinearity, *Phys. Rev. Lett.* **121**, 123601 (2018).
- [22] T. M. Stace, C. H. W. Barnes, and G. J. Milburn, Mesoscopic one-way channels for quantum state transfer via the quantum Hall effect, *Phys. Rev. Lett.* **93**, 126804 (2004).
- [23] A. C. Mahoney, J. I. Colless, L. Peeters, S. J. Pauka, E. J. Fox, X. Kou, L. Pan, K. L. Wang, D. Goldhaber-Gordon, and D. J. Reilly, Zero-field edge plasmons in a magnetic topological insulator, *Nat. Commun.* **8**, 1836 (2017).
- [24] A. C. Mahoney, J. I. Colless, S. J. Pauka, J. M. Hornibrook, J. D. Watson, G. C. Gardner, M. J. Manfra, A. C. Doherty, and D. J. Reilly, On-chip microwave quantum Hall circulator, *Phys. Rev. X* **7**, 011007 (2017).

- [25] R. Kwende, T. White, and O. Naaman, Josephson parametric circulator with same-frequency signal ports, 200 MHz bandwidth, and high dynamic range, *Appl. Phys. Lett.* **122**, 224001 (2023).
- [26] R. Navarathna, D. T. Le, A. R. Hamann, H. D. Nguyen, T. M. Stace, and A. Fedorov, Passive superconducting circulator on a chip, *Phys. Rev. Lett.* **130**, 037001 (2023).
- [27] A. Fedorov, N. P. Kumar, D. T. Le, R. Navarathna, P. Pakkiam, and T. M. Stace, Nonreciprocity and circulation in a passive Josephson-junction ring, *Phys. Rev. Lett.* **132**, 097001 (2024).
- [28] J. Koch, A. A. Houck, K. L. Hur, and S. M. Girvin, Time-reversal-symmetry breaking in circuit-QED-based photon lattices, *Phys. Rev. A* **82**, 043811 (2010).
- [29] C. Müller, S. Guan, N. Vogt, J. H. Cole, and T. M. Stace, Passive On-Chip superconducting circulator using a ring of tunnel junctions, *Phys. Rev. Lett.* **120**, 213602 (2018).
- [30] D. T. Le, C. Müller, R. Navarathna, A. Fedorov, and T. M. Stace, Operating a passive on-chip superconducting circulator: Device control and quasiparticle effects, *Phys. Rev. Res.* **3**, 043211 (2021).
- [31] Y. Takeda, Y. Tabuchi, S. Tamate, S. Masuda, S. Kono, and Y. Nakamura, Passive on-chip microwave circulator based on a Josephson ring, *APS March Meeting Abstracts* (2023), Vol. 2023, pp. T71–005.
- [32] A. E. Miroshnichenko, S. Flach, and Y. S. Kivshar, Fano resonances in nanoscale structures, *Rev. Mod. Phys.* **82**, 2257 (2010).
- [33] S. Fan, W. Suh, and J. D. Joannopoulos, Temporal coupled-mode theory for the fano resonance in optical resonators, *J. Opt. Soc. Am. A* **20**, 569 (2003).
- [34] J. M. Kreikebaum, K. P. O'Brien, A. Morvan, and I. Siddiqi, Improving wafer-scale Josephson junction resistance variation in superconducting quantum coherent circuits, *Supercond. Sci. Technol.* **33**, 06LT02 (2020).
- [35] A. Osman, J. Simon, A. Bengtsson, S. Kosen, P. Krantz, D. Perez, M. Scigliuzzo, J. Bylander, and A. F. Roudsari, Simplified Josephson-junction fabrication process for reproducibly high-performance superconducting qubits, *Appl. Phys. Lett.* **118**, 064002 (2021).
- [36] J. B. Hertzberg, E. J. Zhang, S. Rosenblatt, E. Magesan, J. A. Smolin, J.-B. Yau, V. P. Adiga, M. Sandberg, M. Brink, J. M. Chow, and J. S. Orcutt, Laser-annealing Josephson junctions for yielding scaled-up superconducting quantum processors, *npj Quantum Inf.* **7**, 129 (2021).
- [37] J. Combes, J. Kerckhoff, and M. Sarovar, The slh framework for modeling quantum input-output networks, *Adv. Phys. X* **2**, 784 (2017).
- [38] K. Kalashnikov, W. T. Hsieh, W. Zhang, W.-S. Lu, P. Kamenov, A. Di Paolo, A. Blais, M. E. Gershenson, and M. Bell, Bifluxon: Fluxon-parity-protected superconducting qubit, *PRX Quantum* **1**, 010307 (2020).
- [39] V. Ambegaokar and A. Baratoff, Tunneling between superconductors, *Phys. Rev. Lett.* **10**, 486 (1963).
- [40] T. Walter, P. Kurpiers, S. Gasparinetti, P. Magnard, A. Potočnik, Y. Salathé, M. Pechal, M. Mondal, M. Oppliger, C. Eichler, and A. Wallraff, Rapid high-fidelity single-shot dispersive readout of superconducting qubits, *Phys. Rev. Appl.* **7**, 054020 (2017).
- [41] A. A. Clerk, M. H. Devoret, S. M. Girvin, F. Marquardt, and R. J. Schoelkopf, Introduction to quantum noise, measurement, and amplification, *Rev. Mod. Phys.* **82**, 1155 (2010).
- [42] Z. Zhao, C. Guo, and S. Fan, Connection of temporal coupled-mode-theory formalisms for a resonant optical system and its time-reversal conjugate, *Phys. Rev. A* **99**, 033839 (2019).
- [43] BlueFors, Data sheet for low-loss bulkhead infrared filter, <https://bluefors.com/products/measurement-infrastructure/ir-filter/>.